

Non-Interrupting Rail Track Geometry Measurement System Using UAV and LiDAR

Lihao Qiu, Ming Zhu, JeeWoong Park, Yingtao Jiang, Hualiang (Harry) Teng

Abstract

The safety of train operations is largely dependent on the health of rail tracks, necessitating regular and meticulous inspection and maintenance. A significant part of such inspections involves geometric measurements of the tracks to detect any potential problems. Traditional methods for track geometry measurements, while proven to be accurate, require track closures during inspections, and consume a considerable amount of time as the inspection area grows, causing significant disruptions to regular operations. To address this challenge, this paper proposes a track geometry measurement system (TGMS) that utilizes an unmanned aerial vehicle (UAV) platform equipped with a light detection and ranging (LiDAR) sensor. Integrated with a state-of-the-art machine-learning-based computer vision algorithm, and a simultaneous localization and mapping (SLAM) algorithm, this platform can conduct rail geometry inspections seamlessly over a larger area without interrupting rail operations. In particular, this semi- or fully automated measurement is found capable of measuring critical rail geometry irregularities in gauge, curvature, and profile with sub-inch accuracy. Cross-level and warp are not measured due to the absence of gravity data. By eliminating operational interruptions, our system offers a more streamlined, cost-effective, and safer solution for inspecting and maintaining rail infrastructure.

Keywords

TGMS, UAV, LiDAR, machine learning, SLAM

Introduction

The safety of rail, as a critical component of modern national infrastructure, is paramount due to its far-reaching implications for both the economy and public well-being. Consequently, railway tracks need to be regularly inspected for potential issues. Over time, large forces at the wheel-rail contact points, along with other factors such as weather conditions, natural wear and tear, and track defects, can cause geometric irregularities in the tracks [1]. These irregularities may deviate tracks from their designed performance and compromise their integrity, directly affecting the dynamic response of railway vehicles running on those tracks [2]. This can result in disturbing noises due to increased vibrations, reduced passenger comfort due to rough rides [3], and even catastrophic derailments if left unchecked [4]. To address these challenges, a number of rail track geometry measurement technologies have emerged, many of which are now widely used in the rail industry.

The dominant methods of measuring rail track geometry use Track Geometry Measurement System (TGMS) [8], including manual measurements with specialized tools and automated measurements using various mounts and sensors. While these methods are widely utilized in the rail industry [29], they each have their limitations. Despite being accurate, manual measurements are

cumbersome, labor-intensive, and inefficient, especially when assessing long stretches of track infrastructure spanning hundreds of kilometers. On the other hand, automated sensor-based TGMS provide more efficient measurements over long distances, enabling more convenient monitoring and inspection of long-range track geometry [30]. However, the TGMS requires the closure of rail sections under inspection, which interrupts normal train operations and reduces transportation efficiency.

This study aims to design a TGMS capable of scanning long stretches of track without disrupting normal rail operations. To achieve this, an unmanned aerial vehicle (UAV) is selected as the carrier for the measurement tools and electronics, and a Light Detection and Ranging (LiDAR) sensor is utilized as the major distance measurement tool. The collected data is processed via semantic segmentation for automatic annotation, LiDAR simultaneous localization and mapping (SLAM) for rail scene reconstruction, regression fittings for outlier rejection, and regression fittings for gauge, curvature, and profile measurement. cross-level and warp are not measured in this study due to absence of gravity information.

Literature review

This section introduces the track geometry parameters to measure, research in automated TGMS, and Machine Learning (ML) as well as SLAM techniques

in rail related area.

Track geometry parameters

Common geometric irregularities of railway tracks include deviations in the distance between the rails at one location (i.e., gauge), differences in the height of the two rails at one location (i.e., cross-level), irregular vertical displacements of the rails at different locations (i.e., warp), deviations from the intended shape of the rail tops (i.e., profile or vertical curve), and curvature of the track [5]. These irregularities can be assessed by measuring key geometric parameters of the rails, allowing for maintenance and adjustments to ensure optimal track conditions.

In measurement, gauge is the distance between the inner sides of rail heads measured at 15.875 mm ($5/8$ of an inch) below the top of the rail, as shown in Figure 1 (a). Rail curvature is measured as the mid-ordinate gap between the chord (18.89 m, 62 ft) placed on the side of rail head and the rail, as depicted in Figure 1 (b). Rail profile is measured as the mid-ordinate gap between the chord (18.89 m on top of the rail) and the rail vertically, as shown in Figure 1 (c). Cross-level is measured as vertical distance between the two rails at the same location assisted with a bubble-type level as depicted in Figure 1 (d). Warp is measured as the cross-level between any two points within an 18.89 m span Figure 1 (e).

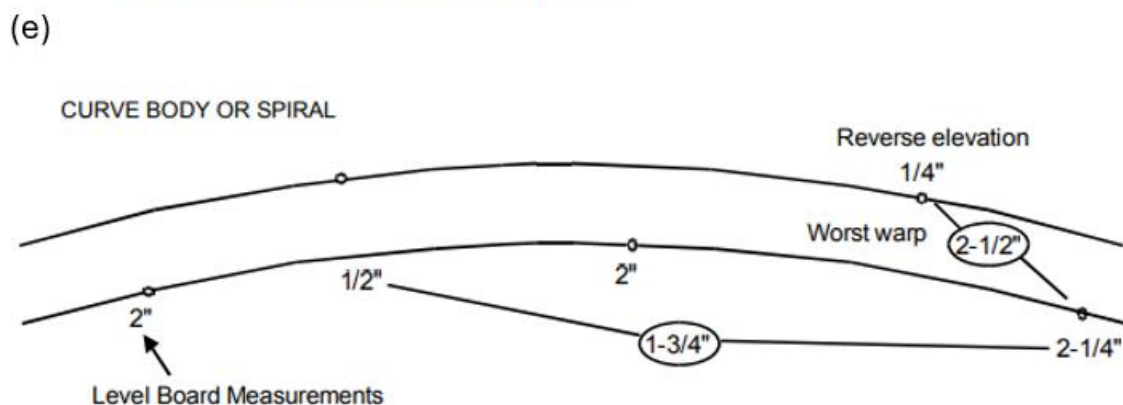
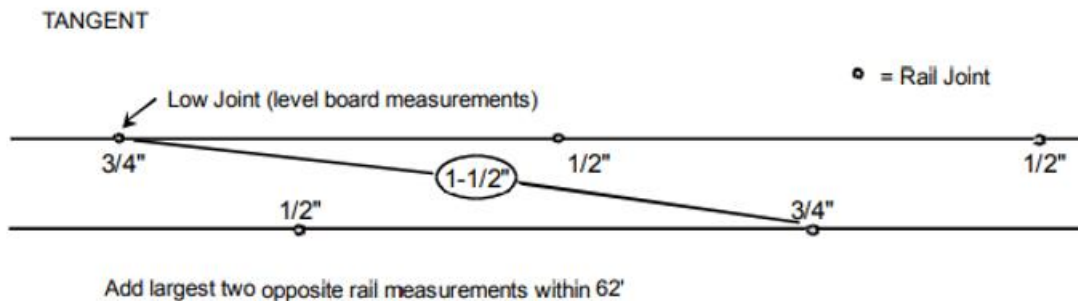
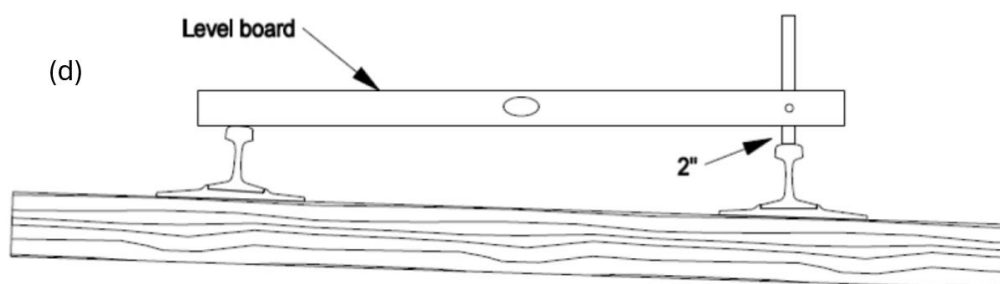
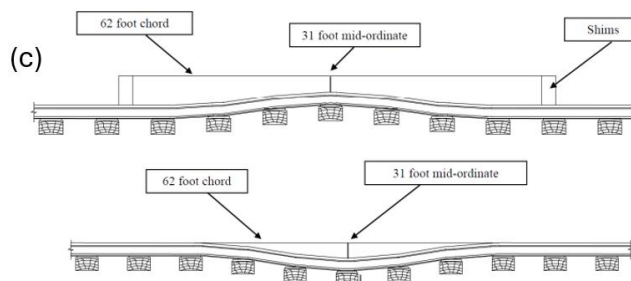
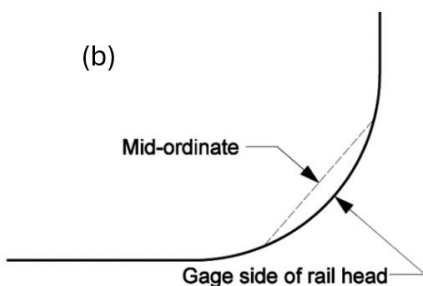
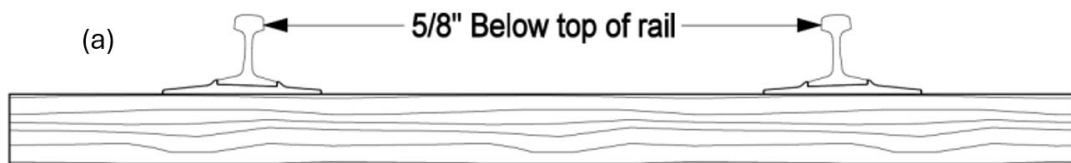


Figure 1 Measurements of rail geometries. (a) Gauge. (b) Curvature. (c) Profile. (d) Cross-level. (e) Warp [6].

TGMS

Track geometry measurement system can measure the track irregularities with electronic device installed on inspection vehicle rolling over track. Typical devices are inertial measurement units (IMUs), global navigation satellite systems (GNSS), and ML technologies.

Extensive research has been carried out regarding TGMS. For instance, Escalona et al. [33] developed a TGMS incorporating kinematics from multibody dynamics analysis to accurately measure track geometric irregularities. This system demonstrated good agreement with traditional methods, showcasing its effectiveness in calculating geometric irregularities using sensor data and computer vision systems. Naganuma et al. [35] introduced a trolley-mounted TGMS equipped with gyroscopes, which measure seven track geometry parameters with high accuracy and repeatability. Utilizing the innovative 'differential-difference method, the system outperforms conventional trolleys with moving parts. Another trolley-mounted TGMS integrated with INS and geodetic surveying equipment [36], due to its modular design, offers versatile configurations for various surveying tasks.

One of the primary advantages of these ATGMS is their ability to provide

continuous and real-time monitoring of track conditions. This enables the early detection of track defects, which can help prevent accidents and reduce maintenance costs. However, there are several challenges associated with the implementation of these systems. One significant issue is the closure of the track when being inspected, which can disrupt rail services and cause significant logistical and financial challenges.

Machine learning in rail related applications

Machine learning is a branch of artificial intelligence involves algorithms learning from data to make predictions or decisions without being explicitly programmed [34]. Although ML is not extensively used in TGMS, many studies in the railway sector apply ML for data analysis. For example, Zhang et al. [16] proposed a novel workflow for reconstructing railway overhead wires from airborne LiDAR data. This method integrates deep learning for wire identification and the RANSAC algorithm for wire reconstruction, achieving higher accuracy in wire identification and reconstruction. Lim et al. [**Error! Reference source not found.**] developed an object detection system for railway safety using ML, specifically implementing a Single-Shot multibox Detection (SSD) MobileNet model. This system effectively detects and classifies various objects in images and real-time video feeds.

SLAM in rail related applications

Simultaneous localization and mapping is a process used in robotics and autonomous systems to build a map of an unknown environment while simultaneously keeping track of the agent's location within that environment [28]. This involves using various sensors, such as cameras, LIDAR, and IMUs, to collect data about the surroundings and then employing certain algorithms, including feature extraction, feature matching, to integrate these multiple sources of data into a coherent map [32]. Though not widely adapted in TGMS, several studies in the rail sector have explored the application of camera-based and/or LiDAR-based SLAM systems. For instance, Wang et al. [19] integrated data from LiDAR, camera, IMU, and GNSS that are mounted on a locomotive to register PCD of the rail environment, achieving a low error rate when compared to the true trajectory. Dai et al. [20] proposed a LiDAR SLAM system for mapping rail tunnels using locomotive-mounted LiDAR data with encouraging performance in repeated environments.

Materials and methods

This chapter introduces the test site, the hardware platform for data acquisition, the data collection process, and the data analysis process (i.e., software) to determine rail geometries.

Test site

The data collection was carried out at the Nevada State Railroad Museum located in Boulder City, Nevada, USA. An almost 210 m test section of mostly straight and slightly curved rail track was selected for this experiment, as shown in Figure 2. This was the only available track section at the museum for experiment and data collection.



Figure 2 Test site at the Nevada State Railroad Museum, Boulder City, Nevada

Measurement equipment / Hardware

The platform hardware includes a DJI Matrix 600 as the carrier, an Ouster OS-1 LiDAR for point cloud data generation, a 3DM-GQ7 IMU for flight status tracing, and an Nvidia Jetson Xavier Development Kit (or Jetson in short) for on-board data acquisition and processing, as shown in Figure 3.

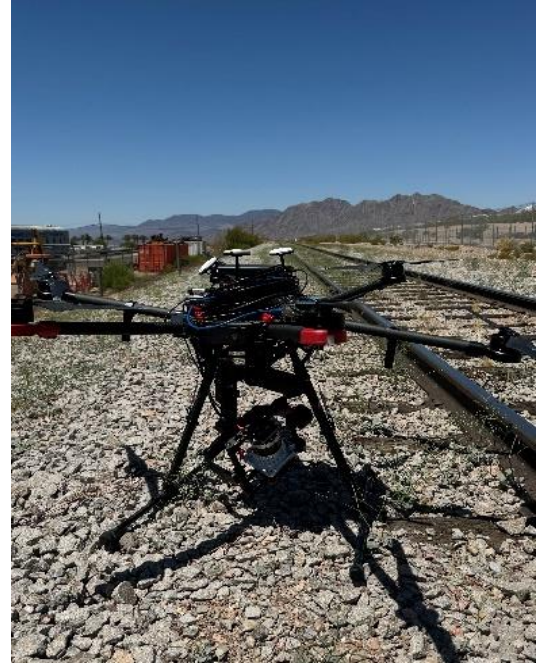
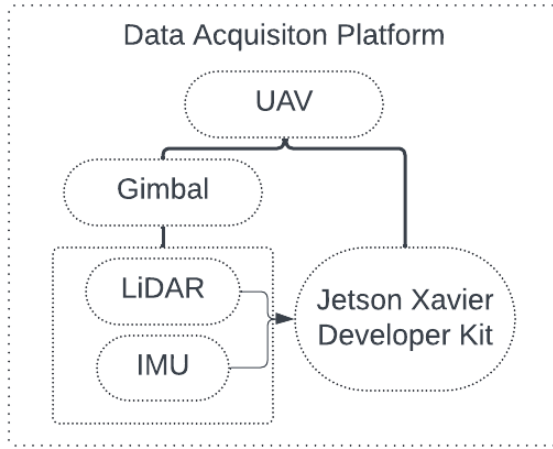


Figure 3 Data acquisition platform.

This UAV spans a dimension of 1668 mm \times 1518 mm \times 759 mm after propellers, frame arms, and GPS mount are unfolded. It can carry the LiDAR with its gimbal mount, the IMU and the Jetson (a total payload of about 6 kg) for a continuous 20-minute flight. The maximum takeoff weight is around 15 kg.

The Ouster OS-1 time-of-flight (ToF) LiDAR scans with a 360° rotational field of view (FOV) horizontally and emits 128 laser channels covering 45°FOV vertically. This LiDAR outputs point cloud data in 3D Cartesian coordinates (x_L, y_L, z_L) that represent the surfaces of surround objects along with their corresponding reflection intensity measurements. Each point is linked to a channel angle, corresponding channel ID ranging from 1 to 128, an azimuth value spanning from 0° to 360°, and timestamps. All other key specifications are provided in Table 1.

Table 1 LiDAR key specifications.

Specifications	Values
Range	0.5m - 170 m
Vertical resolution	32, 64, or 128 points
Horizontal resolution	512, 1024, or 2048 points
Rotation rate	10 or 20 Hz
Vertical FoV	45°
Angular sampling accuracy	±0.01°
False positive rate	1/10,000
Range resolution	0.1 cm

The IMU is attached on top of the LiDAR to accurately capture the instant dynamic posture of the LiDAR via high-speed accelerometers and gyroscopes. The accelerometers measure linear acceleration along three orthogonal axes (x_I, y_I, z_I), while the gyroscopes measure the angular velocity around each of the three axes. All key specifications are detailed in Table 2.

Table 2 IMU key specifications.

Specifications	Accelerometer	Gyroscope
Maximum value	±8 g	±300°/s
Random walk	20 $\mu\text{g}/\sqrt{\text{Hz}}$	0.15°/ $\sqrt{\text{h}}$
Bias instability	5 μg	1.5°/h
Noise density	20 $\mu\text{g}/\sqrt{\text{Hz}}$	8.75°/h/ $\sqrt{\text{Hz}}$

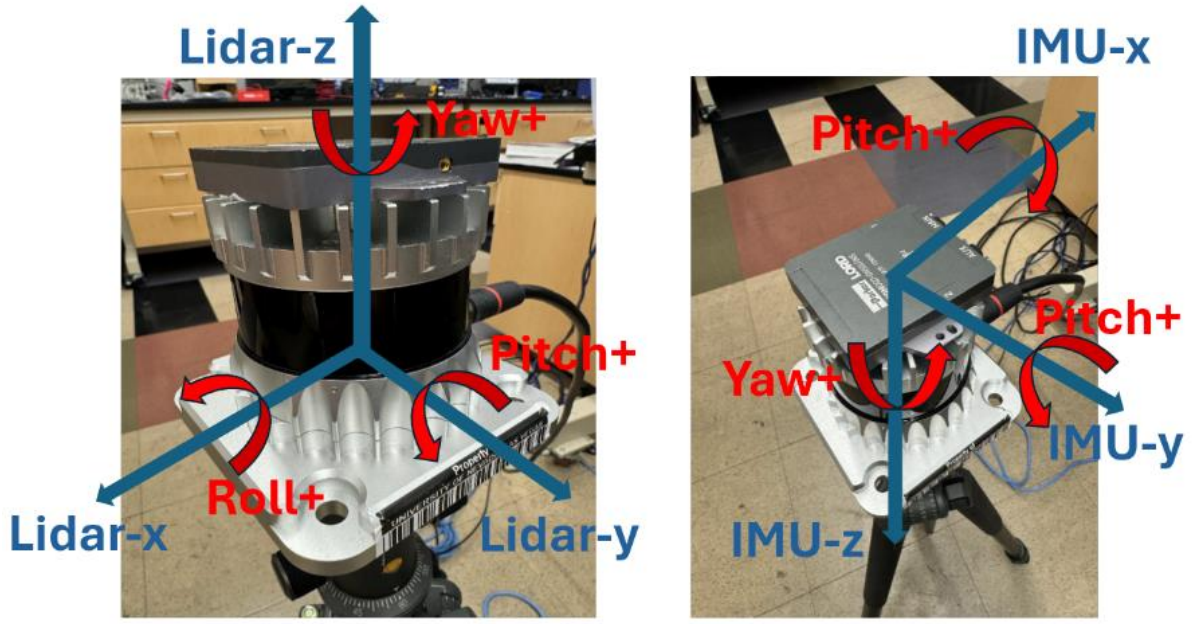


Figure 4 Coordinate difference between LiDAR and IMU.

It is important to note that the axes of the LiDAR correspond to the axes of the IMU, but they are not the same, as depicted in Figure 4. Actually, LiDAR's $x+$ axis coincides with the IMU's $x-$, the LiDAR's $z+$ coincides with the IMU's $z-$, the LiDAR's pitch $+$ coincides with the IMU's roll $+$, and the LiDAR's roll $+$ coincides with the IMU's pitch $-$. Therefore, the IMU coordinate system needs to be projected onto the LiDAR coordinate system using the following equations:

$$\begin{bmatrix} x_L \\ y_L \\ z_L \end{bmatrix} = \begin{bmatrix} -1 & 0 & 0 \\ 0 & 1 & 0 \\ 0 & 0 & -1 \end{bmatrix} \begin{bmatrix} x_I \\ y_I \\ z_I \end{bmatrix} \quad (1)$$

$$\begin{bmatrix} R_L \\ P_L \\ Y_L \end{bmatrix} = \begin{bmatrix} 0 & -1 & 0 \\ 1 & 0 & 0 \\ 0 & 0 & 1 \end{bmatrix} \begin{bmatrix} R_I \\ P_I \\ Y_I \end{bmatrix} \quad (2)$$

where x , y , and z stands for x , y , and z -axis of each sensor, while R stands for roll, P stands for pitch, and Y stands for yaw, respectively. The subscript L and I

stands for LiDAR coordinate and IMU coordinate, respectively.

The Jetson, which serves as the on-board data acquisition and processing unit because of its computational capacity for high-speed, large-volume data transmission, and its compatibility with Robot Operating System (ROS), is employed for automated data collection and processing.

Data collection

The data collection process directly impacts the quality of the measurements. During a data collection session, the UAV flight speed was set to approximately 1 meter per second (m/s), and the altitude was maintained between 3 to 5 meters above the ground to ensure adequate point density for illustrating the rail surfaces. The UAV flew along three different paths: 1) between the test tracks, 2) about 2 meters north of the test track, and 3) about 2 meters south of the test track, thereby scanning all three surfaces (i.e., top and sides) of the test tracks. Each flight mission had an approximate flight time of 15 minutes. The LiDAR operated at a frequency of 10 Hz, with a horizontal resolution of 1024 points and a vertical resolution of 128 points, ensuring dense point cloud coverage on the track surface. The IMU was configured to operate at 500 Hz. Data from both sensors were streamed synchronously via ROS to the Jetson.

Data analysis / Software

Raw PCD frames include both rails (i.e., object of interests) and other surrounding objects that are of no interests. Thus, to enable automated rail geometry measurement, we need to first semantically segment rail tracks from other background objects (e.g., buildings, grounds, trees, stationary facilities, etc.) in PCD frames to identify rail surfaces, and register small vertical FOV PCDs for large-scale curvature/profile measurement. Then, outliers are identified and removed from the dataset, which eliminates any points that were incorrectly classified during the segmentation process. In the end, multiple rail geometric parameters will be calculated. General flow of the data analysis procedure is depicted as in

Figure 5.

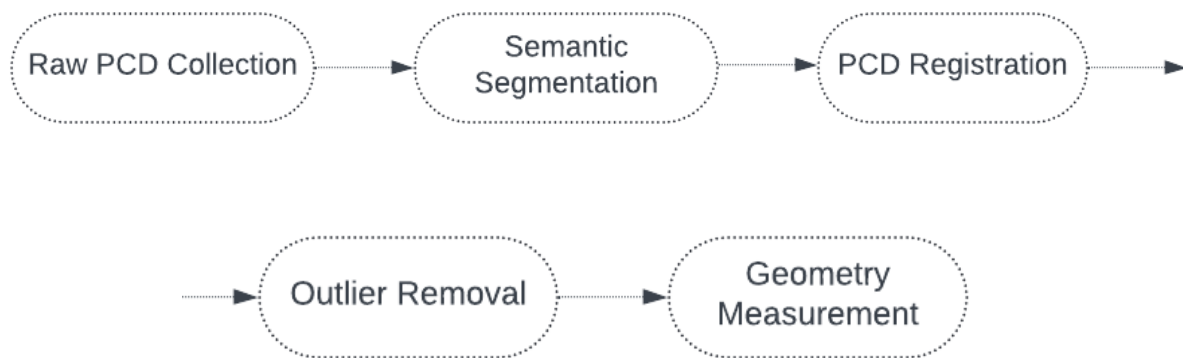


Figure 5 Flowchart for data processing

Semantic segmentation To enable automatic and accurate segmentation of railway point clouds for a variety number of scenarios, a machine learning algorithm should be exploited. However, as aforementioned, there lacks a

publicly accessible point cloud dataset for accurate rail geometry measurement. Therefore, a point cloud dataset with relatively dense point cloud on the rails must be established. To do so, the original LiDAR data stream was decoded and saved as PCD files for annotation. An open source PCD annotation tool, Supervisely [21], was adopted to label rails in each PCD frame, as depicted in Figure 6 (a), where a cuboid was positioned to minimally encapsulate points that represent a rail. Other unlabeled points are considered as background. As a result, 358 PCD frames have been labeled as the ground truth in the dataset. Since the majority of the data only contains two tracks, cropping was performed to preserve the rail points while eliminating most of the background points. Figure 6 (b) illustrates a labeled and cropped PCD frame, with the rail points distinctly highlighted in red.

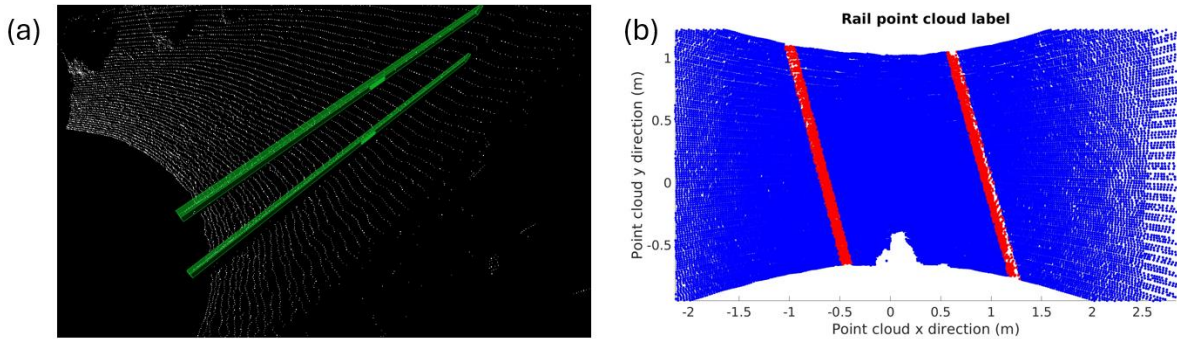


Figure 6 (a)Using cuboid to annotate rail points. (b) Annotated and cropped rail point cloud frame.

To increase the diversity of training samples, data augmentation techniques such as rotation and translation were applied to the original labeled frames [22]. Eventually, 358 labeled PCD frames were augmented to a total of 1,322 frames for the entire rail PCD dataset. The dataset was further split with a 0.7:0.2:0.1

ratio for training, validation, and testing purposes, respectively.

Meanwhile, a machine-learning-based semantic segmentation neural network for 3D PCD [23] is adopted and optimized for automated segmentation of rail points. The network follows an encoder-decoder structure with skip connections. In the encoding stage, random sampling modules contribute to downsampling the number of points, where local spatial encoding (LocSE) modules and attentive pooling (AP) modules aggregate point features to maintain information of unselected points. The LocSE module selects one point p_i with feature f_i in the point cloud and calculate its K neighboring points $[p_i^1, p_i^2, \dots, p_i^K]$ in terms of their relative point position information

$$r_i^k:r_i^k = MLP(p_i \oplus p_i^k \oplus (p_i - p_i^k) \oplus ||p_i - p_i^k||) \quad (3)$$

where $k = [1, 2, \dots, K]$, MLP stands for multi-layer perceptron, \oplus stands for concatenation, and $|| \cdot ||$ calculates the Euclidean distance. The information r_i^k are then concatenated to the feature of point p_i (i.e., $\hat{f}_i^k = f_i \oplus r_i^k$), introducing a new set of neighboring features $\hat{F}_i = [\hat{f}_i^1, \hat{f}_i^2, \dots, \hat{f}_i^K]$. Since the numbers of points in the two classes (i.e., "rail" and "background") are severely imbalanced, where only 1-2 % of the total points belong to rails, a more aggressive downsampling ratio was adopted to decrease the effect of background points when training the neural network. The AP module is used to aggregate the set of neighboring point features \hat{F}_i . The attention score s_i^k is computed through a shared MLP layer followed by *softmax* function:

$$s_i^k = \text{softmax}(\text{MLP}(\hat{f}_i^k, W)) \quad (4)$$

where W is the learnable weights for the shared MLP layers. The weighted features are then calculated as:

$$\tilde{f}_i = \sum_{k=1}^K (\hat{f}_i^k \cdot s_i^k) \quad (5)$$

In the decoder stage, up-sampling modules and multi-layer perceptron (MLP) are used to predict the label for each point in the original PCD frame. In the end, the cross entropy with logits is employed to compute the loss function between predicted labels of each point cloud and its ground truth:

$$\text{loss}_i = - \sum_{j=0}^1 y_{i,j} \cdot \ln p_{i,j} \quad (6)$$

where y_{ij} stands for the ground truth for the j th point in the i th frame, and p_{ij} stands for the prediction for the j th point in the i th frame. The final result is achieved by minimizing all losses. To further address the data imbalance issue, a heavier penalty is put on the rail points predicted as background points. The overall structure of the network structure used is shown in Figure 7.

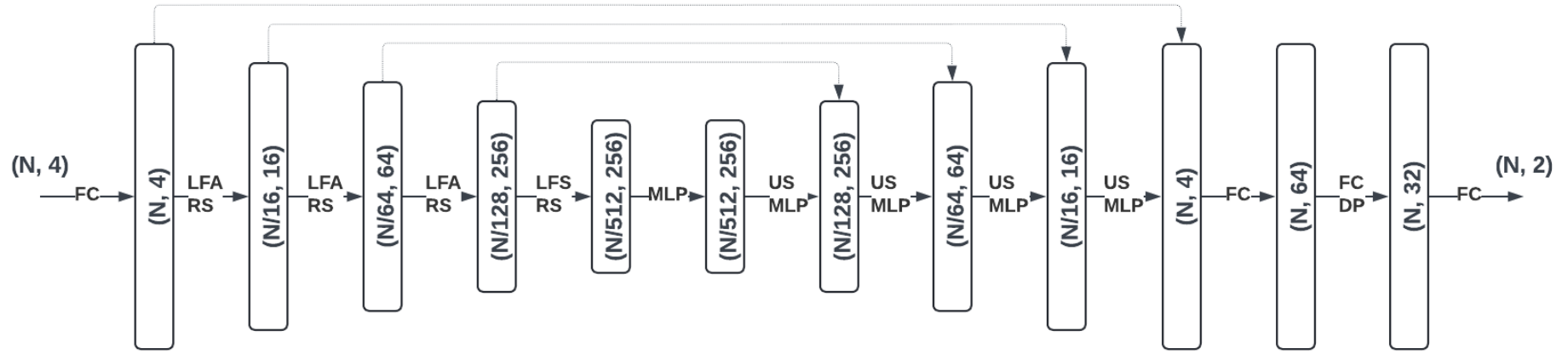


Figure 7 Network structure. (N, F) stands for N points and F dimension of features. FC: fully connected layer. LFA: local feature aggregation. LFA consists of multiple LocSE and AP modules. RS: random sampling. MLP: multi-layer perceptron. US: up-sampling. DP: dropout layer.

Point cloud registration

For rail track curvature and profile measurements that require the rail length no less than 18 m, the FOV of a single PCD frame does not suffice. Therefore, multiple PCD frames need to be stitched into a single coordinate system to generate a larger scene for curvature and profile measurement. To achieve this goal, a SLAM algorithm [24] is exploited to register rail PCD frames utilizing IMU kinematic readings (i.e. acceleration a_t and angular velocity w_t) and engineered point cloud features.

IMU Kinematics

Raw IMU readings are presented as follows:

$$\hat{w}_t = w_t + b_t^w + n_t^w \quad (7)$$

$$\hat{a}_t = R_t^{BW}(a_t - g) + b_t^a + n_t^a \quad (8)$$

where \hat{w}_t and \hat{a}_t represent the noisy readings from the IMU in world frame at time t . These readings are interfered by a slowly varying bias b_t and white noise n_t . R_t stands for the rotation matrix from world coordinate W system to body coordinate system B , and g stands for the constant gravity vector in world coordinate system.

The velocity, position, and rotation of the LiDAR at time $t + \Delta t$ can be

computed as follows:

$$v_{t+\Delta t} = v_t + g\Delta t + R_t(\hat{a}_t - b_t^a + n_t^a)\Delta t \quad (9)$$

$$p_{t+\Delta t} = p_t + v_t\Delta t + \frac{1}{2}g\Delta t^2 + \frac{1}{2}R_t(\hat{a}_t - b_t^a + n_t^a)\Delta t^2 \quad (10)$$

$$R_{t+\Delta t} = R_t^{WB} \exp((\hat{w}_t - b_t^w - n_t^w)\Delta t) \quad (11)$$

The preintegrated IMU method, as described in [25], is then applied to obtain the incremental body motion (i.e., velocity, position, rotation) between two timestamps:

$$\Delta v_{i,j} = R_i^T(v_j - v_i - g\Delta t_{i,j}) \quad (12)$$

$$\Delta p_{i,j} = R_i^T(p_j - p_i - v_i\Delta t_{i,j} - \frac{1}{2}g\Delta t_{i,j}^2) \quad (13)$$

$$\Delta R_{i,j} = R_i^T R_j \quad (14)$$

These values are jointly updated with point cloud feature matching.

Point Cloud Features

Point cloud features are selected by calculating the roughness of each point $p_{i,k}$ (k th point in the i th frame):

$$c_{i,k} = \frac{1}{|S| \cdot \|p_{i,k}\|} \|\sum_{j \in S, j \neq k} (p_{i,k} - p_{i,j})\| \quad (15)$$

where S stands for the set of points surrounding $p_{i,k}$ on the same horizontal channel, with equal number of points on each side of $p_{i,k}$. Points with high roughness are considered as edge features, and points with low roughness are

treated as planar features. A voxel map containing features from previous n frames is used for feature matching. A new scan F_{i+1} with edge feature F_{i+1}^e and planar feature F_{i+1}^p is matched to the voxel map through planar to planar, edge to edge matching. This matching is calculated through equations:

$$d_{e_k} = \frac{|(p_{i+1,k}^e - p_{i,u}^e) \times (p_{i+1,k}^e - p_{i,v}^e)|}{|p_{i,u}^e - p_{i,v}^e|} \quad (16)$$

$$d_{p_k} = \frac{|(p_{i+1,k}^p - p_{i,u}^p) \times (p_{i+1,k}^p - p_{i,w}^p)|}{|(p_{i,u}^p - p_{i,v}^p) \times (p_{i,u}^p - p_{i,w}^p)|} \quad (17)$$

where d_{e_k} represents the distance between the edge point $p_{i+1,k}^e$ to a line formed by the corresponding edge points $p_{i,u}^e$ and $p_{i,v}^e$, d_{p_k} represents the distance between the planar point $p_{i+1,k}^p$ and the plane formed by corresponding planar points $p_{i,u}^p$, $p_{i,v}^p$, and $p_{i,w}^p$. Gauss-Newton method is used to solve for the optimal transformation by minimizing the combined distance among all edge and planar features:

$$\min_{T_{i+1}} \{ \sum_{p_{i+1,k}^e \in \hat{F}_{i+1}^e} d_{e_k} + \sum_{p_{i+1,k}^p \in \hat{F}_{i+1}^p} d_{p_k} \} \quad (18)$$

where \hat{F}_{i+1} represents features transformed with preintegrated relative pose values. This optimization procedure calculates the best estimate of the actual posture change between two specific frames so as to align them in the world coordinate.

Outlier rejection

After the PCD segmentation to extract rails from background and applying the SLAM to expand the FOV, a relatively comprehensive landscape of rails is obtained. Yet, some outliers labeled as “rail points” still need to be removed. First, to ease the subsequent data cleaning and calculations, all “rail” points in the registered point cloud map are rotated using the principal component analysis (PCA) so that the longitudinal direction of the rail points aligns with the x -axis, the lateral width of the track aligns with the y -axis, and the height of the track aligns with the z -axis. The rails are then divided into segments around 5 m long, and each segment is then rotated using PCA again so that they align with the new x , y , z -axis as mentioned above. A quadratic regression

$$y = ax^2 + bx + c \quad (19)$$

where a , b , and c are coefficients, is used for fitting rail points in the x - y plane, and another quadratic regression for the x - z plane to approximate each track respectively. The distance of each point to these two regressions in each plane is then calculated. Points with distance greater than a determined threshold are removed.

Geometry measurement Manual geometry measurement requires identifying specific points or surfaces on the rail. To achieve this, polynomial regressions are employed to determine the rail surfaces in the registered point cloud data (PCD) map for measuring gauge, curvature, and profile. Additionally, a sliding window

method is used to select critical measurement points and to obtain more continuous measurement.

Track gauge measurement

To simulate the standard method of measuring track gauge, we need to first identify the rail head, then locate the rail inner surface 15.875 mm (i.e., 5/8 of an inch) below the top of the rail head. We select the top 10% of the points in each segment and average their average z-values to approximate the rail head. Then, the innermost 10% of the rail points that are 15.75 – 16 mm beneath the top of rail head are selected as the inner rail surface points for track gauge measurement. Because PCD data are innately sparse, direct measurement would be difficult. As an alternative, two linear regressions are fitted to interpolate these surface points. A 5-meter long sliding window is then used to select the critical points, where $(x_{1,1}, y_{1,1}), (x_{1,2}, y_{1,2})$ are two points on one linear regression line that are 5 meters apart, and $(x_{2,1}, y_{2,1}), (x_{2,2}, y_{2,2})$ are the ones 5 meters apart on the other linear regression line (Figure 8). The sliding gauge value is then calculated as the distance between two midpoints of both linear regression line segments (i.e., $(x_{1,m}, y_{1,m}) = ((x_{1,1} + x_{1,2})/2, (y_{1,1} + y_{1,2})/2)$ and so forth) [26]:

$$d_g = \sqrt{(x_{1,m} - x_{2,m})^2 + (y_{1,m} - y_{2,m})^2} \quad (20)$$

and the window shifts 0.5 m at a time to minimize non-linearity and ensure continuity.

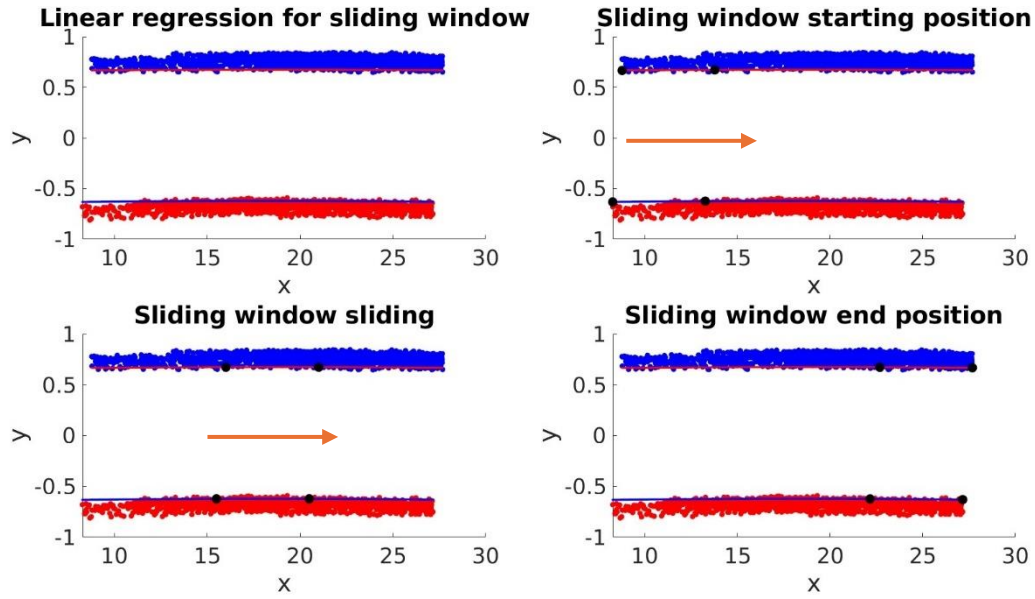


Figure 8 Sliding window demonstration. TL: linear regression line for gauge. TR: five-meter sliding window starting point. BL: sliding window in process. BR: sliding window stop position.

Track curvature measurement To accurately determine track curvature, points along the gauge side of the rail head should be identified and used to approximate the manual measurement method (Figure 1 (b)). Nevertheless, due to the sparse nature of PCD, this approach can lead to inaccurate regression fitting. Instead, all rail head points within a 18.89 m-long window are used for regression fitting in the x-y plane.

The top 10% of the rail points within each window are selected and fitted with a quadratic regression in the x-y plane that represents the gauge side of the reference rail. The points at both ends of the window are fitted with a linear regression to approximate the 62-foot chord in the x-y plane. The rail curvature

for that section is then calculated as the lateral distance between the quadratic and the linear regressions at the window's midpoint. This window slides at a 3 m-step every time along the track for each subsequent calculation, providing a continuous measurement of curvature along the track.

Profile measurement Similar to calculating track curvature, points representing rail heads should be identified for measuring profile. Within each data window, the top 10% of points are selected to represent the rail head. In the x-z plane, these points are fitted with a quadratic curve, while the points at both ends are fitted with straight lines. The track profile measurement for that section is determined by calculating the vertical distance between the quadratic curve and the linear fits at the window's midpoint. This process is repeated as the window moves along the track at 3 m each time, providing a continuous profile measurement.

Results

This section presents the intermittent results from semantic segmentation, PCD registration, outlier removal, and the calculated track gauge, curvature, and profile using geometry measurement.

Semantic segmentation result

The precision of the track geometry calculations depends heavily on the accuracy of the semantic segmentation process. During the training process, the batch size is set to eight, and the learning rate is set to 0.01. Given the significant imbalance between the two classes of points in rail PCD, the Intersection over Union (IoU) metric is employed to assess the model's performance, rather than traditional metrics such as accuracy or F1-score. After the training and validation process (Figure 9), the model demonstrated a highest IoU of 82.4%.

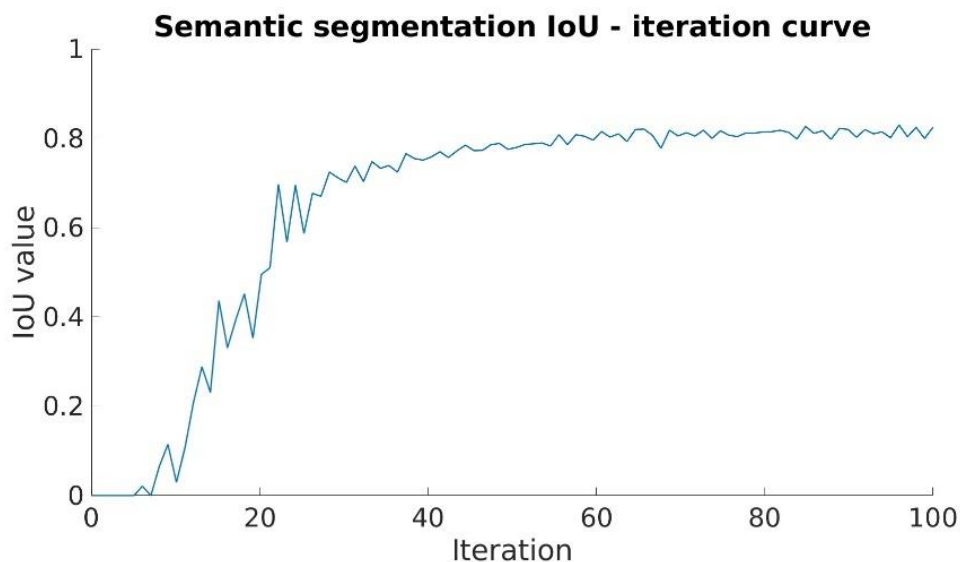


Figure 9 IoU value during testing.

Point cloud registration result

The process of point cloud registration involves aligning and merging successive LiDAR frames to create a comprehensive, detailed composite representation of the test site. Figure 10 presents the registered point cloud data of the test site. This figure showcases the effectiveness of the registration process,

with the rails prominently highlighted in red. This coloration is based on the predicted labels, clearly distinguishing the rails from other elements within the scene.

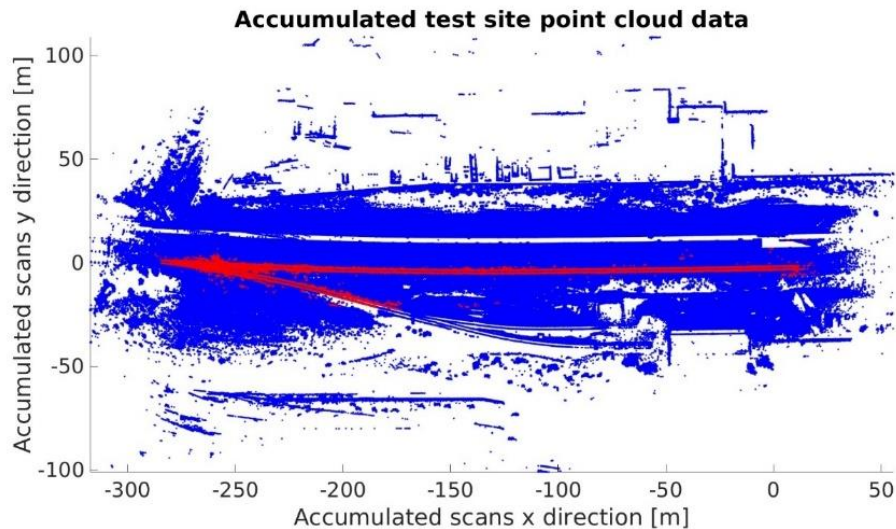


Figure 10 Registration result

Outlier rejection result

Outliers in the registered map can significantly affect measurement accuracy. To address this, outliers are removed using the distance-based method aforementioned. Specifically, thresholds of 7 cm in the x-y plane and 8 cm in the x-z plane are applied, based on visual inspection post-outlier removal. In this dataset, 10,511 outliers were identified and removed from a total of 50,503 rail points.

Geometry measurement result

All measurement results are compared to the field measurement using specialized rail track tools, as depicted in Figure 11. The track gauge was measured at every 5 meters where the track curvature and the profile were measured at 18.89 m (i.e., 62 feet) apart, with 11 measurements in total. All field measurements started at the landmark position as shown in Figure 11. The measurement results from the platform are then compared to the field measurement results when each sliding window location aligns with the on-field measurement location.

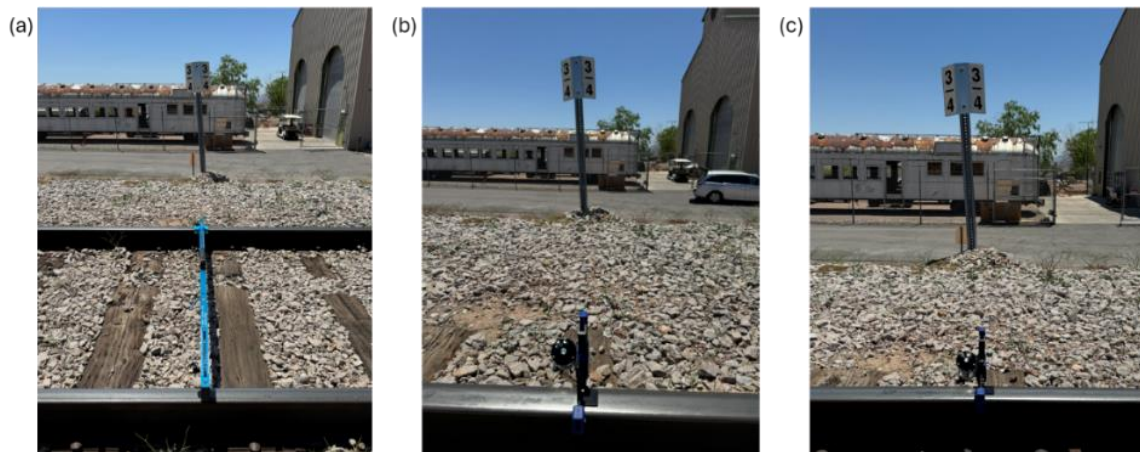


Figure 11 Rail Measurement. (a) Measuring gauge from the landmark using gauge measuring tool. (b) Measuring curvature from the landmark using curvature measuring tool. (c) Measuring profile from the landmark using profile measuring tool.

Track Gauge

Gauge is measured at 15.875 mm below the top of the rail head. Figure 12

illustrates the gauge measurement process in the PCD that simulates this measurement method. The inner surface is identified by locating it approximately 15.75-16 mm below the rail head. Figure 15 (a) presents a histogram of deviations between these two sets of gauge measurements. Notably, around 78.57% of these deviations are within 2cm.

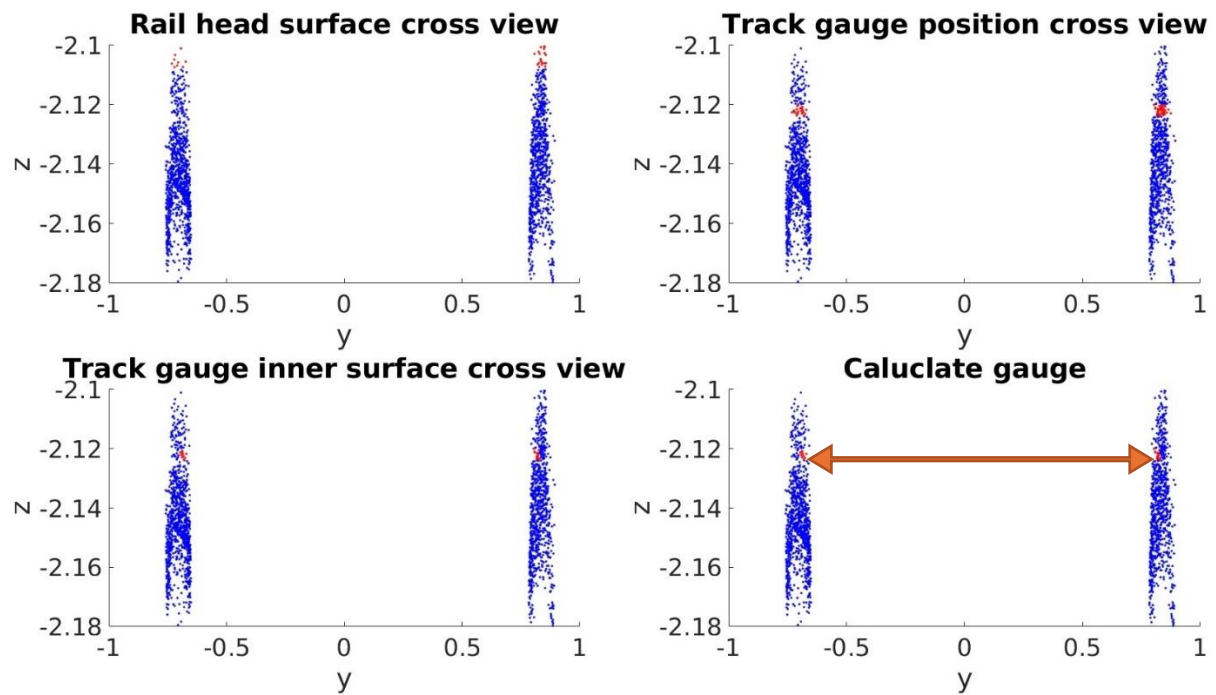


Figure 12 Gauge calculation process. (TL) Selecting rail head. (TR) Finding 15.75 – 16 mm below rail head. (BL) Finding inner surface. (BR) Calculating gauge.

Track Curvature

Track curvature is assessed by measuring the gap at the midpoint between the 18.89 m chord and the gauge side of the reference rail. Figure 13 illustrates the

curvature measurement process that simulates this method by fitting a linear regression as the chord and a quadratic regression at the gauge side of the reference rail in the x-y plane. Figure 15 (b) shows the histogram depicting the deviations between the measured curvature and the calculated curvature values. Overall, 77.27% of the deviations fall within 1 cm.

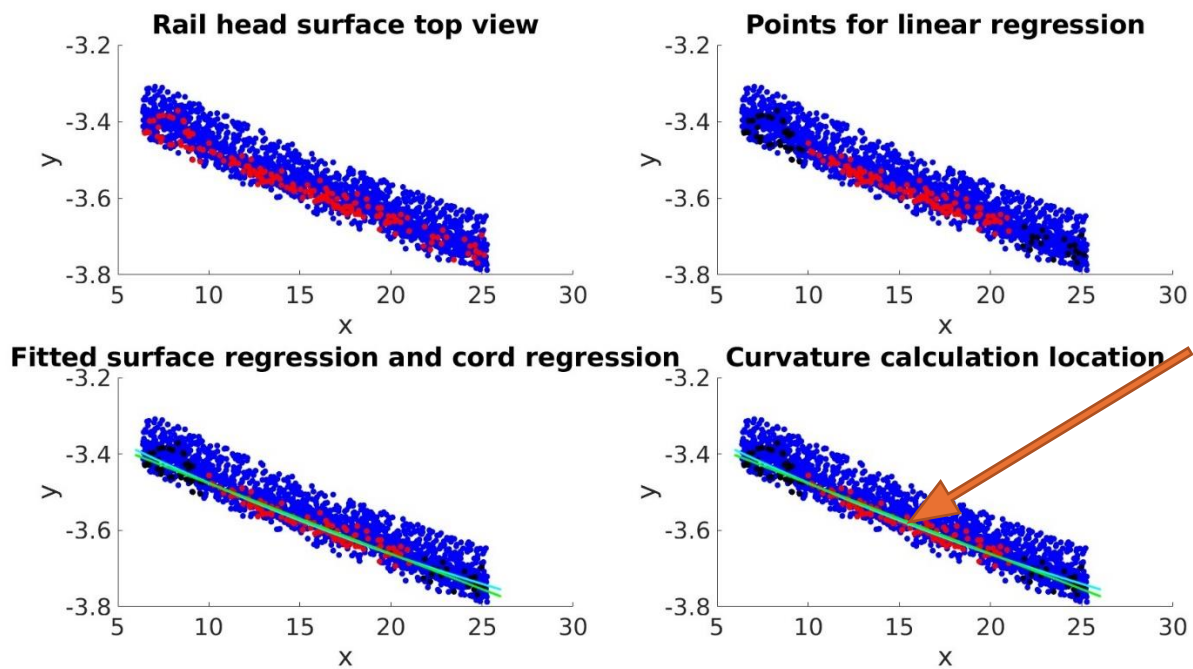


Figure 13 Track curvature calculation process. (TL) Finding rail head points. (TR) Finding the points on both ends for chord simulation. (BL) Fitting the surface regression and the cord regression. (BR) Calculating the gap at the midpoint.

Track Profile

Track profile is measured by placing an 18.89 m string line along the top of the reference rail and measuring the distance from the midpoint of the string line to

the top of the reference rail. Figure 14 demonstrates the profile measurement in the rail points through fitting a linear regression as the string line and a quadratic regression as the top of the reference rail in the $x - z$ plane. Figure 15 (c) depicts a histogram of the deviations between the measured profile values and the calculated profile values, where 77.27% of the deviations fall within 1 cm.

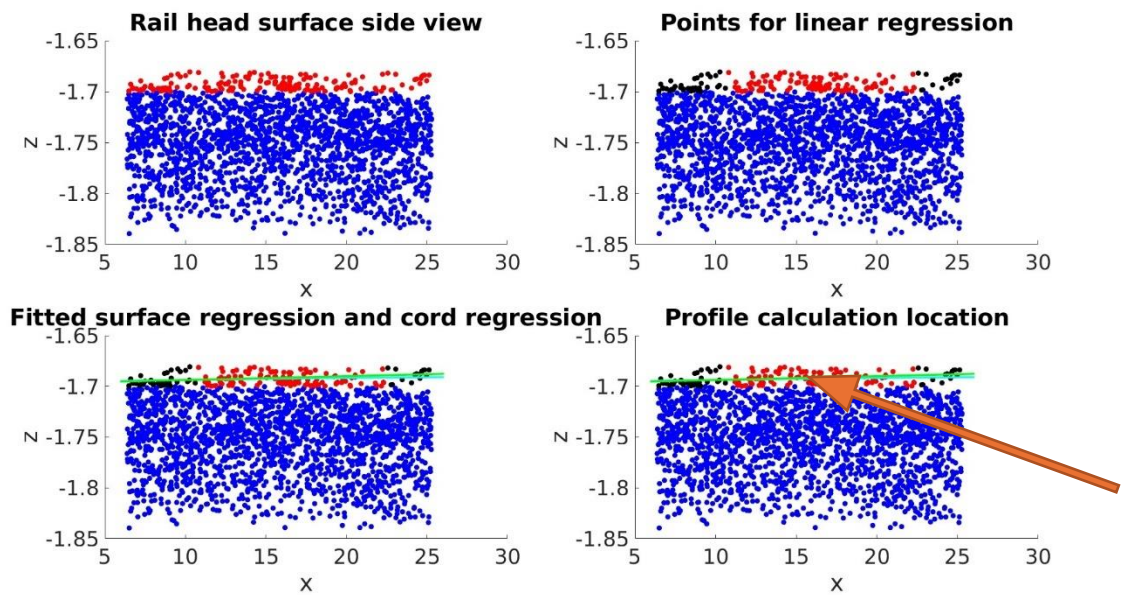


Figure 14 Profile calculation. (TL) Finding rail head. (TR) Finding chord location. (BL) Fitting rail head and chord. (BR) Calculating profile gap

Table 3 Part of ground truth and measurement result. GT: ground truth. Mt.: measurement. L: Left rail. R: Right rail. Left rail is the one to the south. All units are shown in cm.

Case	Gauge GT	Gauge Mt.	Curvature GT (L/R)	Curvature Mt. (L/R)	Profile GT (L/R)	Profile Mt. (L/R)
1	143.5	144.5	0.15/0.47	0.37/0.12	0.80/0.00	1.15/0.00
2	143.8	143.5	2.06/2.38	2.04/2.00	0.60/0.90	0.00/0.85

3	143.5	143.5	1.91/2.06	1.94/1.22	1.40/0.90	0.13/0.14
4	144.1	145.2	0.64/0.64	0.41/0.07	1.90/1.50	0.00/0.29
5	144.5	144.2	0.16/0.16	0.70/0.63	0.20/0.60	0.85/0.51

Table 3 presents a sample of the ground truth and measured results. All measurements are in unit centimeter (cm).

Table 4 shows the mean, the standard deviation (Std), the root mean square error (RMSE), and the average relative error percentage (AREP) of all three calculations. Although the RMSE values for all three calculations are similar, the gauge measurement demonstrates a notably lower AREP value. Given that the measured gauge values are around 1.435 m, the relative error percentage for the gauge is only approximately 0.77%. In contrast, for curvature and profile, the relative error percentages are notably higher.

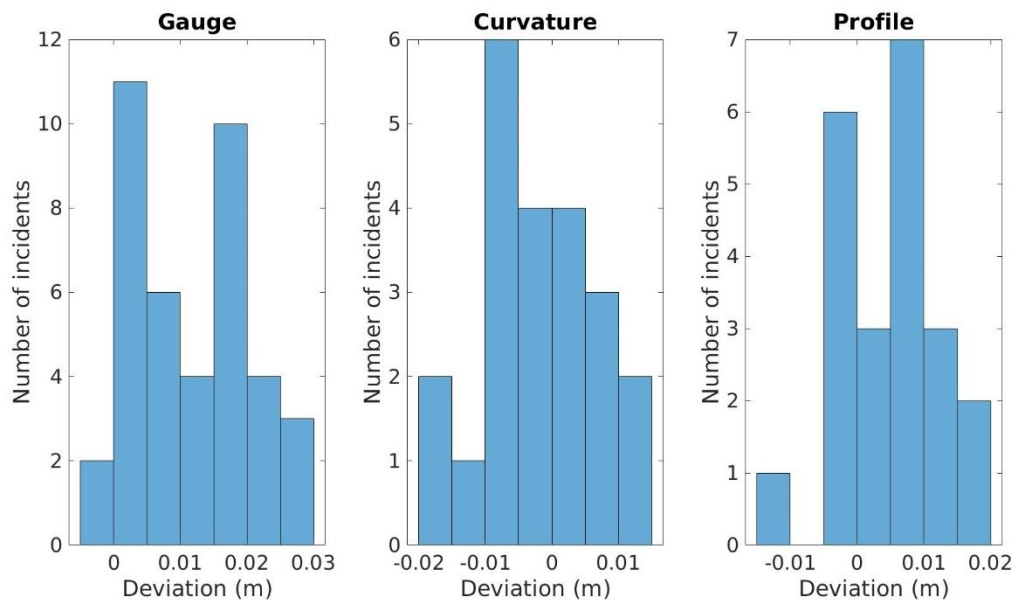


Figure 15 Histogram of: (a) Gauge difference. (b) Curvature difference. (c) Profile difference.

Table 4 Platform calculation result summary.

Parameter	Mean (cm)	Std (cm)	RMSE (cm)	AREP
Gauge	144.88	1.68	1	0.77%
Curvature	0.97	0.84	0.84	143.77%
Profile	0.124	0.35	0.87	111.20%

Discussion

The results presented in this work highlight the potential of the proposed system for measuring railroad track geometries. Specifically, track gauge measurement demonstrated high accuracy, with an RMSE of 1 cm and an AREP of 0.77%. However, the system showed larger deviations when measuring track curvature and profile, with AREP values exceeding 100%. One potential factor is that the test tracks are predominantly straight, resulting in minimal curvature or profile variation, which leads to a higher AREP. Testing on curved sections could yield different results.

The current system relies solely on point cloud data and lacks information regarding the direction of gravity at each point. Consequently, it is unable to measure cross-level and warp values accurately. Future enhancements should focus on integrating appropriate sensors or algorithms to capture these parameters effectively, thereby improving the precision of existing measurements. This advancement is essential for advancing the system's capabilities in track geometry measurement.

Conclusion

This paper presented an innovative rail track geometry measurement platform capable of conducting inspections alongside normal rail operations. Utilizing a UAV platform equipped with a LiDAR sensor and an on-board data acquisition system, the proposed approach integrates a state-of-the-art machine-learning-based computer vision algorithm for rail point segmentation and a LiDAR SLAM algorithm for expanding the point cloud field of view. Through the application of regression techniques for outlier removal and precise geometry calculations, the platform has demonstrated high accuracy in measuring critical rail geometry parameters, including gauge, curvature, and profile, with sub-inch precision. Compared to traditional field measurements using specialized tools, our system significantly reduces operational interruptions, offering a more streamlined, cost-effective, and safer solution for inspecting and maintaining rail infrastructure. Future work will focus on enhancing measurement accuracy further and incorporating additional assessments such as cross-level and warp evaluations to broaden the platform's capabilities.

Acknowledgement

The authors would like to thank the Nevada State Railroad Museum for the test site they provided and their collaboration. This work was supported by U.S. Department of Transportation University Transportation Program with contract number 69A3551747132.

Declaration of conflicting interest

The author(s) declared no potential conflicts of interest with respect to the research, authorship, and/or publication of this article.

Reference

1. Cannon DF, Edel KO, Grassie SL, Sawley K. Rail defects: an overview. *Fatigue & Fracture of Engineering Materials & Structures*. 2003 Oct;26(10):865-86.
2. Iwnicki S. *Handbook of railway vehicle dynamics*. CRC press; 2006 May 22.
3. Sadeghi J, Khajehdezfuly A, Heydari H, Askarinejad H. Development of railway ride comfort prediction model: Incorporating track geometry and rolling stock conditions. *Journal of Transportation Engineering, Part A: Systems*. 2020 Mar 1;146(3):04020006.
4. Zhang Y, Han J, Song H, Liu Y. Subway embedded track geometric irregularity safety limits. *Chinese Journal of Mechanical Engineering*. 2021 Dec;34:1-0.

5. Federal railroad administration track safety standards fact sheet.
<https://railroads.dot.gov/divisions/railroad-safety/track-safety-standards>,
2013.
6. Federal Railroad Administration. Track Safety Standards Compliance Manual. Federal Railroad Administration, 1 April 2007,
<https://www.fra.dot.gov>. Archived from the original (PDF) on 28 May
2008. Retrieved 13 November 2012.
7. Tsunashima H, Naganuma Y, Kobayashi T. Track geometry estimation
from car-body vibration. Vehicle System Dynamics. 2014 May
30;52(sup1):207-19.
8. Farkas A. Measurement of railway track geometry: A state-of-the-art
review. Periodica Polytechnica Transportation Engineering.
2020;48(1):76-88.
9. Chen Q, Niu X, Zuo L, Zhang T, Xiao F, Liu Y, Liu J. A railway track
geometry measuring trolley system based on aided INS. Sensors. 2018 Feb
10;18(2):538.
10. Escalona JL, Urda P, Muñoz S. A track geometry measuring system based
on multibody kinematics, inertial sensors and computer vision. Sensors.
2021 Jan 20;21(3):683.
11. Wang X, Pan H, Guo K, Yang X, Luo S. The evolution of LiDAR and its
application in high precision measurement. In IOP Conference Series: Earth

and Environmental Science 2020 May 1 (Vol. 502, No. 1, p. 012008). IOP Publishing.

12. Arastounia M. Automated recognition of railroad infrastructure in rural areas from LiDAR data. *Remote Sensing*. 2015 Nov 6;7(11):14916-38.
13. Arastounia M. An enhanced algorithm for concurrent recognition of rail tracks and power cables from terrestrial and airborne lidar point clouds. *Infrastructures*. 2017 Jun 2;2(2):8.
14. Sahebdivani S, Arefi H, Maboudi M. Rail track detection and projection-based 3D modeling from UAV point cloud. *Sensors*. 2020 Sep 13;20(18):5220.
15. Geng Y, Pan F, Jia L, Wang Z, Qin Y, Tong L, Li S. UAV-LiDAR-based measuring framework for height and stagger of high-speed railway contact wire. *IEEE Transactions on Intelligent Transportation Systems*. 2021 May 24;23(7):7587-600.
16. Zhang L, Wang J, Shen Y, Liang J, Chen Y, Chen L, Zhou M. A deep learning based method for railway overhead wire reconstruction from airborne LiDAR data. *Remote Sensing*. 2022 Oct 21;14(20):5272.
17. Manier A, Moras J, Michelin JC, Piet-Lahanier H. Railway lidar semantic segmentation with axially symmetrical convolutional learning. *ISPRS Annals of the Photogrammetry, Remote Sensing and Spatial Information Sciences*. 2022 May 17;2:135-42.

- 18.Lin S, Xu C, Chen L, Li S, Tu X. LiDAR point cloud recognition of overhead catenary system with deep learning. Sensors. 2020 Apr 14;20(8):2212.
- 19.Wang Y, Song W, Lou Y, Zhang Y, Huang F, Tu Z, Liang Q. Rail vehicle localization and mapping with LiDAR-vision-inertial-GNSS fusion. IEEE Robotics and Automation Letters. 2022 Jul 12;7(4):9818-25.
- 20.Dai X, Song W, Wang Y, Xu Y, Lou Y, Tang W. LiDAR-Inertial Integration for Rail Vehicle Localization and Mapping in Tunnels. IEEE Sensors Journal. 2023 Jun 20.
- 21.Supervisely. Supervisely Computer Vision platform. Supervisely Ecosystem [Internet]. Supervisely; 2023 Jul [cited 2023 Jul 20]. Available from: <https://supervisely.com>
- 22.Maharana K, Mondal S, Nemade B. A review: Data pre-processing and data augmentation techniques. Global Transitions Proceedings. 2022 Jun 1;3(1):91-9.
- 23.Hu Q, Yang B, Xie L, Rosa S, Guo Y, Wang Z, Trigoni N, Markham A. Randla-net: Efficient semantic segmentation of large-scale point clouds. InProceedings of the IEEE/CVF conference on computer vision and pattern recognition 2020 (pp. 11108-11117).
- 24.Shan T, Englot B, Meyers D, Wang W, Ratti C, Rus D. Lio-sam: Tightly-coupled lidar inertial odometry via smoothing and mapping. In2020

IEEE/RSJ international conference on intelligent robots and systems (IROS) 2020 Oct 24 (pp. 5135-5142). IEEE.

25. Forster C, Carlone L, Dellaert F, Scaramuzza D. On-manifold preintegration for real-time visual--inertial odometry. *IEEE Transactions on Robotics*. 2016 Aug 31;33(1):1-21.
26. Alexander DC, Koeberlein GM. *Elementary geometry for college students*. Houghton Mifflin; 1999 Jan.
27. Soilán M, Sánchez-Rodríguez A, del Río-Barral P, Perez-Collazo C, Arias P, Riveiro B. Review of laser scanning technologies and their applications for road and railway infrastructure monitoring. *Infrastructures*. 2019 Sep 20;4(4):58.
28. Jixian ZH, Fei LI. Review of visual SLAM environment perception technology and intelligent surveying and mapping application. *Acta Geodaetica et Cartographica Sinica*.;52(10):1617.
29. Saadat S, Stuart C, Carr G, Payne J. FRA autonomous track geometry measurement system technology development: past, present, and future. In *ASME/IEEE Joint Rail Conference 2014 Apr 2* (Vol. 45356, p. V001T05A002). American Society of Mechanical Engineers.
30. Keylin A. *Measurement and Characterization of Track Geometry Data: Literature Review and Recommendations for Processing FRA ATIP Program Data*.

31. Tratman EE. Railway track and track work. Engineering news publishing Company; 1908.
32. Khan MU, Zaidi SA, Ishtiaq A, Bukhari SU, Samer S, Farman A. A comparative survey of lidar-slam and lidar based sensor technologies. In 2021 Mohammad Ali Jinnah University International Conference on Computing (MAJICC) 2021 Jul 15 (pp. 1-8). IEEE.
33. Escalona JL, Urda P, Muñoz S. A track geometry measuring system based on multibody kinematics, inertial sensors and computer vision. Sensors. 2021 Jan 20;21(3):683.
34. Alpaydin E. Machine learning. MIT press; 2021 Aug 17.
35. Naganuma Y, Yada T, Uematsu T. Development of an inertial track geometry measuring trolley and utilization of its high-precision data. International Journal of Transport Development and Integration. 2019 Aug 14;3(3):271-85.
36. Chen Q, Niu X, Zuo L, Zhang T, Xiao F, Liu Y, Liu J. A railway track geometry measuring trolley system based on aided INS. Sensors. 2018 Feb 10;18(2):538.
37. Lim KG, Siruno D, Tan MK, Liao CF, Huang S, Teo KT. Mobile machine vision for railway surveillance system using deep learning algorithm. In 2021 IEEE International Conference on Artificial Intelligence in Engineering and Technology (IICAET) 2021 Sep 13 (pp. 1-6). IEEE.